Super-resolution nanoscopy imaging applied to DNA double-strand breaks

Sofia D'Abrantes, Sarah Gratton, Pamela Reynolds, Verena Kriechbaumer, Joseph McKenna, Stephen Barnard, Dave T. Clarke and Stanley W. Botchway

Published version information:

Citation: S D'Abrantes et al. "Super-resolution nanoscopy imaging applied to DNA double-strand breaks." Radiation Research vol. 189, no. 1 (2017): 19-31.

doi: 10.1667/RR14594.1

RADIATION RESEARCH **189**, 19–31 (2018)
0033-7587/18 $15.00

DOI: 10.1667/RR14594.1

Super-Resolution Nanoscopy Imaging Applied to DNA Double-Strand Breaks

Sofia D'Abrantes,[a] Sarah Gratton,[a] Pamela Reynolds,[b,1] Verena Kriechbaumer,[c] Joseph McKenna,[c] Stephen Barnard,[d] Dave T. Clarke[a] and Stanley W. Botchway[a,2]

[a] *Central Laser Facility, Science and Technology Facilities Council (STFC) Rutherford Appleton, Laboratory, Research Complex at Harwell, Didcot OX11 0QX, United Kingdom;* [b] *Gray Institute for Radiation Oncology and Biology, Department of Oncology, University of Oxford, Oxford OX3 7DQ, United Kingdom;* [c] *Plant Cell Biology, Biological and Medical Sciences, Oxford Brookes University, Oxford OX3 0BP, United Kingdom; and* [d] *Public Health England, Centre for Radiation, Chemical and Environmental Hazards, Chilton, Didcot OX11 0RQ, United Kingdom*

D'Abrantes, S., Gratton, S., Reynolds, P., Kriechbaumer, V., McKenna, J., Barnard, S. Clarke, D.T. and Botchway, S. W. Super-Resolution Nanoscopy Imaging Applied to DNA Double-Strand Breaks. *Radiat. Res.* 189, 19–31 (2018).

Genomic deoxyribonucleic acid (DNA) is continuously being damaged by endogenous processes such as metabolism or by exogenous events such as radiation. The specific phosphorylation of histone H2AX on serine residue 139, described as γ-H2AX, is an excellent indicator or marker of DNA double-strand breaks (DSBs). The yield of γ-H2AX (foci) is shown to have some correlation with the dose of radiation or other DSB-causing agents. However, there is some discrepancy in the DNA DSB foci yield among imaging and other methods such as gel electrophoresis. Super-resolution imaging techniques are now becoming widely used as essential tools in biology and medicine, after a slow uptake of their development almost two decades ago. Here we compare several super-resolution techniques used to image and determine the amount and spatial distribution of γ-H2AX foci formation after X-ray irradiation: stimulated emission depletion (STED), ground-state depletion microscopy followed by individual molecule return (GSDIM), structured illumination microscopy (SIM), as well as an improved confocal, Airyscan and HyVolution 2. We show that by using these super-resolution imaging techniques with as low as 30-nm resolution, each focus may be further resolved, thus increasing the number of foci per radiation dose compared to standard microscopy. Furthermore, the DNA repair proteins 53BP1 (after low-LET irradiations) and Ku70/Ku80 (from laser microbeam irradiation) do not always yield a significantly increased number of foci when imaged by the super-resolution techniques, suggesting that γ-H2AX, 53PB1 and Ku70/80 repair proteins do not fully co-localize on the units of higher order chromatin structure.

INTRODUCTION

The mammalian genome is continuously under attack from both intra- and extracellular processes including cellular metabolism and ionizing radiation, respectively (*1*). Much of the deoxyribonucleic acid (DNA) damage from metabolic processes are single-strand breaks (SSBs) and base lesions, and are repaired with high fidelity. However, DNA damage caused by ionizing radiation, including ultraviolet (UV), X rays, gamma rays and energetic particles, leads to a variety of base damage, SSBs, clusters of lesions including double-strand breaks (DSBs), base–base dimerization and protein-DNA cross-links (*2–5*). Such damage to the genomic DNA of cells can lead to significant errors in transcription and replication if not repaired correctly and may result in mutations, genomic instability and even cell death (*6*). DNA DSBs are thought to be the most deleterious and can initiate genomic instability, ultimately leading to cancer (*1, 6*). The fidelity of repair or misrepair of DSBs is therefore very important to the fate of cells. Thus, radiation has a detrimental effect in addition to its positive therapeutic effect in the treatment of cancer. For this reason, it is essential to closely monitor the techniques, processes and parameters that detect DNA DSBs and cellular integrity.

In recent years, the phosphorylation of the histone protein H2AX, a member of the five histone H2A families, via serine (carboxyl terminus, C4), termed γ-H2AX, is a known indicator of DNA DSB formation, the loss of which is shown to represent DSB repair (*7*). γ-H2AX formation occurs within a few minutes, and maximal signal is estimated to be approximately 30 min after the initial radiation insult (*8*). Depending on the type of damage induced, γ-H2AX can persist for more than 24 h. During the

Editor's note. The online version of this article (DOI: 10.1667/RR14594.1) contains supplementary information that is available to all authorized users.

[1] Current address: Diamond Light Source Ltd., Diamond House, Didcot, OX11 0DE, UK.

[2] Address for correspondence: Science and Technology Facility Council, Central Laser Facility, Rutherford Appleton Laboratory, Harwell, Didcot, Oxon OX11 0QX, UK; email: stan.botchway@stfc.ac.uk.

response to DSBs, phosphorylation of chromatin H2AX molecules extends over kilobase pairs from the DSB, resulting in visible foci formation. As yet it is unknown whether a focus is formed only at a DNA DSB site or if the phosphorylation process leads to unrelated foci formation. γ-H2AX foci formation is thought to be a nonrandom event with lower levels of foci formed in areas of heterochromatin compared with that in euchromatin (*9–11*). The number of foci induced per radiation dose may be used as a sensitive indicator of the radiation treatment or particular cell sensitivity to the ionizing radiation since these are easily detected at low radiation doses (<1 Gy) (*12–14*). The number of γ-H2AX foci formed is also a potential marker for precancerous cells and may be used to monitor cancer treatment effectiveness (*12–14*). However, the large foci spatial distribution within the chromatin, as well as the need for phosphorylation up to 30 Mbp, are not fully understood in relationship to quantifying DNA damage.

The efficiency of DSB repair is currently assessed by monitoring the disappearance of immunohisto-labeled γ-H2AX foci for fixed samples or molecular fluorescent-labeled repair proteins [such as green fluorescent protein (GFP)] for real-time studies (*8*). Reports on the recruitment of repair enzymes to the damage site and DNA-damage response (DDR) signaling processes are important to the understanding of the DNA damage repair mechanisms as a whole, in addition to the effects of radiation in cells and the organism. The repair of radiation-induced DNA damage, including DSBs, is complex and involves the interplay of several signaling processes. Some studies have suggested that the repair pathway choice depends on the complexity in addition to the origin of the DSB (*8, 15*). Although several published studies have indicated that repair proteins are recruited to the sites of damage in live cells, the coordinated repair protein interplay with γ-H2AX and the effect of the DNA DSBs is not well understood (*16, 17*). After DNA DSB formation, a set of phosphatidylinositol-3 kinases (PI3Ks), such as ATM and DNA-PKcs, are activated in concert with several other repair proteins. At least five major signaling pathways operate together for an effective repair. Mammalian cells have developed two key repair pathways: non-homologous DNA end joining (NHEJ) and homologous recombination (HR) (*18*). The former is thought to be the predominant DSB repair pathway in mammalian cells during all phases of the cycle, while the latter operates mainly during the S phase of the cell cycle (*15*). Key NHEJ DSB repair proteins, such as Ku70 and Ku80 that play a critical role in V(D)J recombination, have been shown to co-localize with γ-H2AX in immunohistochemical staining and confocal microscopy studies (*8*). However, the recruitment and disappearance of the Ku and γ-H2AX fluorescence appear to be significantly different.

The p53-binding protein 1 (53BP1) has been identified as a protein that interacts with the central DNA binding domain of p53, a tumor suppressor protein (*19*). 53BP1 is also an important regulator of the cellular response to DSBs and is induced during V(D)J and class switch recombination. 53BP1 is recruited to DNA DSBs, since it is part of the first line of the repair process (*8, 20*). Furthermore, 53BP1 is thought to promote non-homologous DNA end joining-mediated DSB repair while preventing homologous recombination (*20*).

Fluorescence microscopy is an established technique to image DNA DSB foci. Although confocal laser scanning florescence microscopy resolution is typically 250 nm, this is not enough to resolve foci that may be significantly smaller, thus leading to under-scoring of foci and underestimating the effects from DNA damaging agents. Currently, there are a number of different approaches to improve the resolution of epifluorescence and confocal microscopes. The development of super-resolution techniques, such as 4Pi, stimulated emission depletion (STED), ground-state depletion microscopy followed by individual molecule return (GSDIM), structured illumination microscopy (SIM), photo-activated localization microscopy (PALM) and stochastic optical reconstruction microscopy (STORM), to answer several biological questions, offers the opportunity to image DNA damage foci at almost 10× the resolution of confocal microscopes (*21–24*). Co-localization and fluorescence confocal imaging studies of DNA DSB foci of 53BP1 and γ-H2AX show that the spatial resolution afforded by these techniques is too low to sufficiently quantify adjacent or almost overlapping foci. Recently, super-resolution techniques have been used to image both the 2D and 3D structure of DNA (*25–27*). Such studies also include investigating the 3D organization of chromatin in different epigenetic states, revealing distinct chromatin packaging for different epigenetic states at the kilobase to megabase scale, dimensions that are relevant to genome regulation (*28*). A further super-resolution study, in which DNA repair was monitored after laser microirradiation, identified mechanisms of repair pathway choice defined by cellular sensitivities and resistance mechanisms to anticancer agents (*29*). Furthermore, NHEJ proteins such as Ku and XRCC4 that recognize DNA termini *in vitro*, resided within ''microfoci'' along the laser tracks, which contrasted with a broader distribution of γ-H2AX that spreads away from DSB sites. These studies indicate that super resolution should be able to determine whether multiple foci are present within the foci structure resulting from DNA damage going beyond the diffraction-limited foci obtained.

In this study, we used improved confocal microscopy (Airyscan, HyVolution 2) and STED, SIM and GSDIM super-resolution (defined as ≥2× point-spread function) nanoscopy (<100 nm) imaging methods. We observed that after ionizing radiation-induced DNA DSBs, the recruitment of 53BP1 together with the formation of γ-H2AX did not directly co-localize when imaged at a resolution of less than 100 nm. The recruitment of Ku70/80 was also investigated as further evidence of DNA DSB formation. Furthermore, these techniques showed that the number of DNA DSB foci per Gy per cell of radiation dose are likely

to be significantly underestimated by a factor of 3 to 5 when using immunofluorescent labeling in combination with standard confocal fluorescence microscopy.

MATERIALS AND METHODS

Cell Lines, Cell Culture and Irradiations

HeLa cells were cultured in minimum essential medium (MEM) supplemented with 10% fetal bovine serum (FBS), 100 units/ml penicillin, 100 μg/ml streptomycin and 2 m*M* L-glutamine in T75 flasks. Chinese hamster ovary (CHO) cells were cultured in a nutrient mixture of Ham's F-12 medium supplemented with 10% FBS, 100 units/ml penicillin, 100 μg/ml streptomycin and 2 m*M* L-glutamine. Stably Ku80-EGFP-tagged XR-V15B cells (a derivative of CHO cells) were cultured in Ham's F-12 medium supplemented with 10% FBS, 100 units/ml penicillin, 100 μg/ml streptomycin and 2 m*M* L-glutamine. Cells were cultured for 48 h prior to plating at 1.5×10^5 cells/dish in 35-mm diameter, no. 1.5 glass coverslip bottom dishes (MatTek Corp., Ashland, MA) containing 2 ml of complete growth media. After plating, cells were incubated for 24 h at 37°C with 5% CO_2 humidified air in an incubator (Sanyo, Osaka, Japan) to form a monolayer of adherent cells at ~70% confluency determined by visualizing the cells using an inverted microscope (Ceti; Medline Scientific, Chalgrove, UK).

Ultrasoft X-ray irradiations. Ultrasoft X-ray irradiations were performed using the Medical Research Council's ultrasoft X-ray setup at the Oxford Institute for Radiation Oncology (Oxford, UK). This setup is comprised of a cold cathode discharge tube that has an aluminum foil transmission target producing Al_K shell (1.49 keV) ultrasoft X rays with a bremsstrahlung contamination of <1% (*2*). Dosimetry was calculated by Dr. M. Hill using an air-filled ion chamber with a 0.248 mg/cm^{-2} window for the Al_K ultrasoft X rays. The nominal dose rate was approximately 9.5 Gy min^{-1}.

Hard X-Ray Irradiations

Low-linear energy transfer (LET) hard X-ray irradiation was performed at the Health Protection Agency (now Public Health England, Chilton, Didcot, UK), using a 250 kVp X-ray source (AGO X-Ray Ltd., West Coker, UK). Exponentially growing cells plated on MatTek glass bottom dishes for 24 h were irradiated at room temperature. On the day of irradiation, the cells were removed from the incubator and taken to Public Health England where they were exposed to 2 Gy hard X rays (250 kVp, 13.0 mA at 500 mGy/min using both 1 mm copper and 1 mm aluminum filtering. After irradiations, cells were delivered to the culture laboratory and incubated for 20 min, 30 min and 5 h at 37°C with 5% CO^2 humidified air before fixing.

Laser Irradiations

Nonionizing radiation that mimics radiation-induced DNA damage is now well documented (*8, 44*). Exponentially growing attached V15B cells were labeled with 1 μg/ml^{-1} Hoechst (Sigma-Aldrich Co. Ltd., Dorset, UK) at 37°C for 20 min. Laser irradiations were performed using 405 nm (one-photon excitation, 1 mW) at room temperature. The laser light was focused using a 60× (NA 1.2) water immersion objective. The laser beam was fixed and the sample stage was raster scanned in steps of 20 μm. After irradiations, the cells were fixed and immunohisto-labeled for confocal and super-resolution imaging.

Cell Fixation

After irradiations, the cell media was removed from the 35-mm glass or Mylar® dishes and the cells were washed with 1× phosphate buffered saline (PBS). The cells were fixed in 1 ml 4% paraformaldehyde solution (PFA) for 15 min at room temperature. After fixation, the cells were washed 3 times in PBS and stored at 4°C prior to primary and secondary antibody staining.

The Alexa Fluor® 488 and Alexa Fluor 555 dyes have been shown to have excellent properties for almost all the current super-resolution techniques as well as for normal fluorescence microscopy, particularly confocal. Therefore, these were chosen for the studies reported here. The newly developed silicon-rhodamin dye (SiR; see below) specifically developed for super-resolution techniques (STED) was conjugated to the secondary antibody of 53BP1 to allow super resolution in the far red. This dye was chosen for the dual-color/labeled STED and SIM studies (*30*). No dual-labeled GSDIM was performed in this study.

Silicon-Rhodamin Conjugation to 53BP1 Secondary Antibody

The PBS buffer of 1 mg unconjugated goat anti-rabbit antibody (Thermo Fisher Scientific™ Inc., Waltham, MA) was exchanged for 1 ml 0.1 *M* $NaHCO_3$ using a NAP-5 column (GE Healthcare, Buckinghamshire, UK). Solid SiR NHS ester (1 mg; Spirochrome, Stein am Rhein, Switzerland) was dissolved in 100 μl DMSO (Life Technologies, Grand Island, NY) and then added to the antibody solution. The reaction was incubated for 1 h in the dark at room temperature, with occasional agitation. The conjugate was separated from any unreacted SiR NHS ester using a PD-10 column (GE Healthcare). The absorbance of the conjugate at 280 nm and at the maximum absorbance of the dye (652 nm according to Spirochrome) was measured using a Nanodrop 2000c (Thermo Fisher Scientific) and the absorbance of the antibody was calculated using: $A_{protein} = A_{280} - A_{max}(CF_{280})$. Here, A is absorbance, $A_{protein}$ is absorption of tagged protein, A_{280} is the absorbance at 280 nm (absorption maximum of proteins), A_{max} is the absorbance at the absorption maximum of the dye and CF_{280} is the correction factor used in the determination of degree of labeling.

Protein concentration was calculated by assuming 1.4 $A_{protein} = 1$ mg/ml (this value is correct for IgG antibodies). The degree of labeling (*DOL*, dye-to-protein ratio) was then calculated using Eq. (1):

$$DOL = \frac{A_{max}\ x\ MW}{[protein]x\ \varepsilon_{dye}}, \quad (1)$$

where *MW* is molecular weight of tagged protein and ε_{dye} is extinction coefficient of the dye. An average of 7.55 dye molecules per antibody was calculated using this method (see Table 1 for details).

Cell Immunohistochemical Fluorescent Staining

Prior to immunohisto-labeling, the PBS was removed from fixed HeLa, V15B and CHO cells followed by the addition of 1 ml permeabilizing buffer (0.25% Triton™ X-100 in PBS) to each dish and incubated for 5 min at room temperature. Cells were washed 3 times with PBS and incubated for 15 min at room temperature in 1 ml blocking solution (1% BSA in PBS). The blocking buffer was removed before the primary antibody solution was added, and cells were incubated for 45 min at room temperature. The primary antibody solution consisted of 1 μg mouse anti-γ-H2AX antibody (clone JBW301; EMD Millipore, Billerica, MA) and 1 μg rabbit anti-53BP1 (Bethyl Laboratories Inc., Montgomery, TX) made up to 500 μl in blocking buffer. Samples were washed 3 times with PBS and incubated in secondary antibody solution for 30 min in the dark at room temperature. The secondary antibody solution consisted of 1 μg Alexa Fluor 488 donkey anti-mouse (Life Technologies) and 1 μg SiR goat anti-rabbit (see SiR conjugation to secondary antibody, above) made up to 500 μl in blocking buffer. For the V15B cell samples, the primary antibody solution consisted of 1 μg mouse anti-γ-H2AX antibody (clone JBW301; EMD Millipore) and the secondary antibody solution consisted of 1 μg Alexa Fluor 555 goat anti-mouse (Life

TABLE 1
Conjugation of DNA Repair Protein to SiR Dye

A_{280}	A_{max}	Dye CF_{280}	Corrected A_{280}	Protein concentration (mg/ml)	Protein concentration (μM)	Dye concentration (μM)	Dye ε_{max} ($mol^{-1}cm^{-1}$)	Protein A_{280} for 1 mg/ml	Protein *MW*	Dyes per protein molecule
0.4	1.14	0.147	0.23	0.17	1.51	11.4	$1x10^5$	1.4	110,000	7.55

Notes. The degree of labeling (DOL; dye-to-protein ratio) was calculated using Eq. (1), resulting in an average of 7.55 dye molecules per antibody. A = absorbance; A_{280} = absorbance at 280 nm (absorption maximum of proteins); A_{max} = absorbance at the absorption maximum of the dye; CF_{280} = the correction factor used in the determination of DOL; *MW* = molecular weight of tagged protein.

Technologies). Samples were washed 3 times with PBS and stored in the dark at 4°C. Cells were later mounted with ProLong Gold Antifade Mountant (Thermo Fisher Scientific) 24 h prior to confocal and super-resolution microscopy.

Confocal and Super-Resolution Microscopy

Dual-color confocal images of fixed CHO, HeLa and V15B cells irradiated with 2 Gy followed by immunolabeling with primary and secondary antibody fused with Alexa Fluor 488 dye, Alexa Fluor 555 dye and SiR were obtained using the Zeiss Airyscan and Leica SP8 microscopes (Carl Zeiss Microscopy Ltd., Cambridge, UK and Leica Microsystems Inc., Buffalo Grove, IL, respectively). Control samples were treated similarly, but were not irradiated.

Stimulated Emission Depletion Microscopy

Single- and dual-color STED super-resolution microscopy was performed using the Leica SP8 commercial confocal microscope system that integrates the gated TCS STED super-resolution concept. The system uses the nanometer tunable broadband platform of an acousto-optic tunable filter together with an acousto-optical beam splitter (AOBS). In this technique, the point-spread function from a Gaussian beam, transverse mode 00 (TM_{00}), is shaped by the application of a second depletion beam, with TM_{01}, to achieve an improved point-spread function (*PSF*) as described in Eqs. (2) and (3), respectively, shown in Fig. 1. Therefore, the effective point-spread function described by Eq. 2 is modified to Eq. (3).

$$PSF = \frac{\lambda}{2NA} = \frac{\lambda}{2n\ sin\alpha} \tag{2}$$

$$STED\ PSF = \frac{\lambda}{2n\ sin\ \alpha\sqrt{1+\frac{I}{I_{sat}}}}, \tag{3}$$

where PSF is the point-spread function or image resolution, λ is the excitation wavelength, *NA* is the numerical aperture or the refractive index (n) of the medium multiplied by the sine of the angle of incidence, I is the intensity and I_{sat} is the depletion intensity.

Ground-State Depletion Microscopy followed by Individual Molecule Return

The nanoscopic technique of GSDIM provides a detailed map of the spatial arrangement of individual single molecule fluorescence events to form the microscopy image. In this technique, the natural fluorescent dye transferred from a ground state S0 to an excited state S1 following an absorption of quanta or photon and the subsequent oscillation back to the ground state with emission of fluorescent light is significantly reduced by lowering the number of electrons involved in this oscillation cycle by switching most of the fluorescent dye to a dark triplet energy state (*31, 32*). The overall effect of this is to reduce the number of excitable fluorophores in the ensemble population to the single molecule regime. Generally, and as performed here, several thousands of images (frames) are collected using an electron-multiplying charged coupled device (Andor Technology Ltd., Belfast, UK) built into the GSDIM instrument, and the exact localization position of single fluorophores are determined by an algorithm. The Leica GSDIM used in this study operated in the total internal reflection microscopy (TIRF) mode with a lateral resolution (X,Y) specified as being ca 20 nm.

Three-Dimensional-Structured Illumination Microscopy

Structured illumination is a wide-field microscopy technique that projects a grid pattern generated through interference of diffraction orders on the specimen. The Zeiss Elyra used in this work is able to capture three or five images with a set of rotations at an angle of 60°. A complex algorithm is then used to reconstruct the final image by extracting high-frequency components that contain higher resolution, which is otherwise lost in the standard point-spread function, as well as by the blurring from out-of-focus light contributions. The SIM technique does not require any special sample preparation, so the same dishes of irradiated cells were used for all the super-resolution techniques including the SIM technique.

RESULTS

Pseudo-Super-Resolution Imaging of DNA DSBs

The Airyscan (Zeiss LSM 880) is suggested to give a resolution of approximately 150 nm in the lateral dimension and 400 nm axially and may be considered a pseudo-super-resolution technique. We have employed this technique in a comparison to standard confocal microscopy. The Airyscan system was also compared to the currently available super-resolution techniques described here. The advantages of using the Zeiss LSM 880 Airyscan include fast live cell imaging (although not performed here) and the ability to use any fluorophore that can be imaged by epifluorescence or confocal microscopy without any modification.

Figure 2 shows two images for comparison of HeLa cells irradiated with 2 Gy soft X rays followed by immunolabeling with primary and secondary antibody fused with Alexa Fluor 488 and SiR dyes using a combined Zeiss confocal and a Airyscan microscope. It is evident that the improved confocal Airyscan imaging technique yields highly resolved foci that are missing from the confocal image. In practice, the level of resolution obtained with this technique (120 nm with deconvolution; see raw data, Supplementary Fig. S1; http://dx.doi.org/10.1667/RR14594.1.S1) is better than expected since the ''best achievable'' resolution recommended by the manufacturer is approximately 140 nm. The line-width profile across certain parts of the image shows resolutions of approxi-

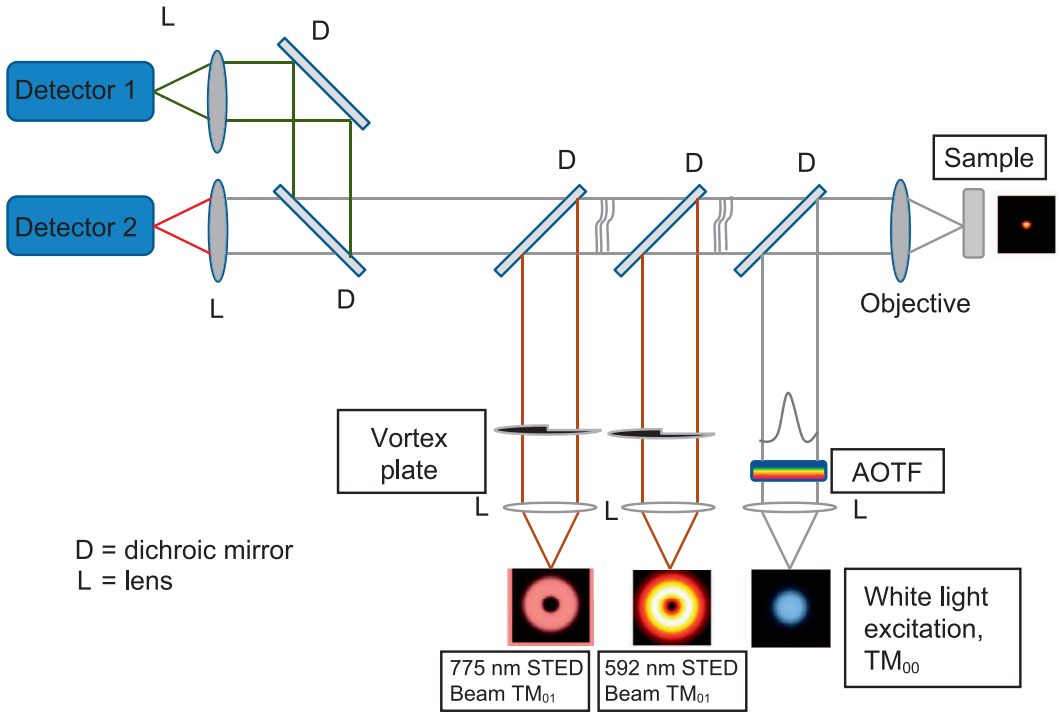

FIG. 1. Schematics of STED nanoscopy.

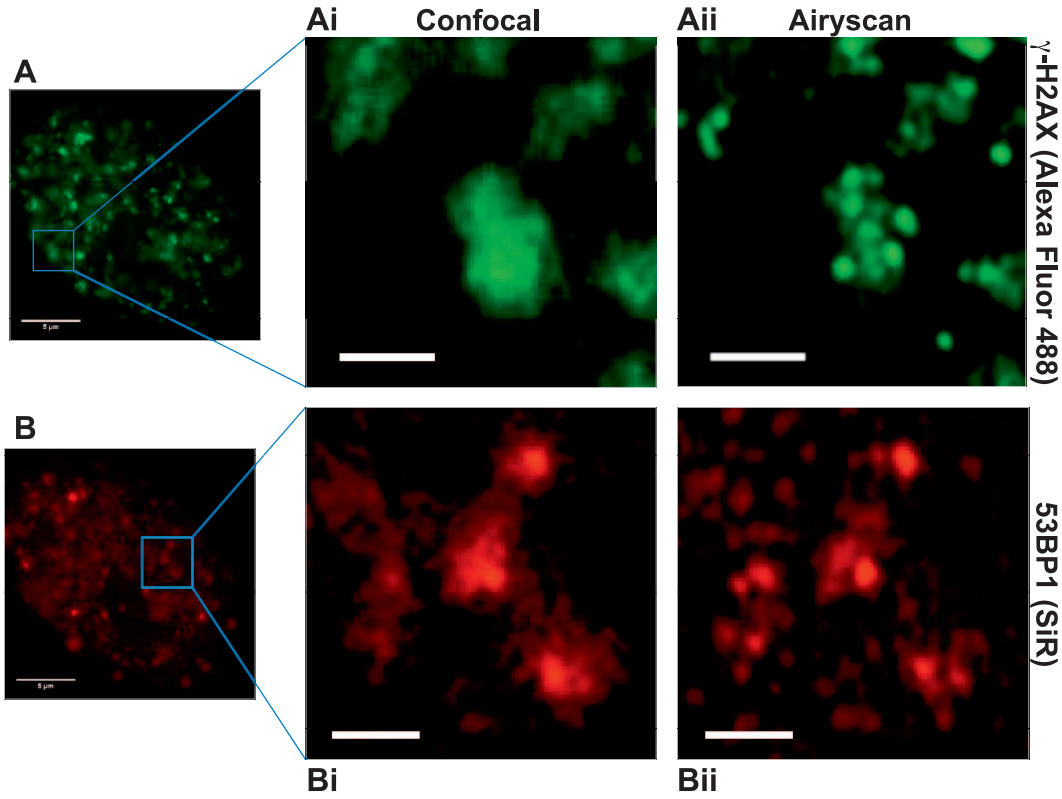

FIG. 2. Fluorescence intensity image of soft X-ray-irradiated HeLa cells labeled with primary and secondary antibody to γ-H2AX and 53BP1. Fluorescently tagged secondary antibody was fused with Alexa Fluor 488 and SiR, respectively. Panels A and Ai: Confocal images of γ-H2AX. Panel Aii: Airyscan super-resolved foci image of panel Ai. Panels B and Bi: Confocal image of 53BP1. Panel Bii: Airyscan super-resolved foci image of panel Bi. Scale bars: 5 μm (panels A and B) and 1 μm (panels Ai, Aii, Bi and Bii).

mately 140–160 nm (shown in Supplementary Fig. S1), while deconvolution gives resolution of approximately 120 nm or less. It is highly likely that the characteristics of the foci structure allow for significantly improved resolution beyond that expected due to the ''point-like'' nature of the foci. For example, the hexagonal 32-channel gallium arsenide phosphide (GaAsP) detector used for the Airyscan acts as an array of pinholes. In general, confocal microscopes achieve improved resolution by reducing sensitivity or closing down the physical pinhole. However, this is at a significant expense of signal sensitivity, so that by reducing the pinhole from, e.g., 1.25 airy units (AU) to 0.2 AU, a drop of 95% of signal is expected as a result (*33*). The 32-array GaAsP avoids the need to reduce the pinhole that leads to signal loss. Each of the elements in the array is approximately 0.2 AU and all together combine to approximately 1.25 AU. More importantly, all 32 elements are mapped and recorded at the same time so that there is an increase in signal sensitivity as well as better localization of the signal position with an effective pinhole of better than 0.2 AU. Additionally, the point-like nature of the foci means the localization precision during the Airyscan deconvolution is more effective than one of an irregular shape. This may lead to the improved resolution of the foci.

Recently, another point-spread function engineering super-resolution method has been introduced by Leica Microsystems called HyVolution 2. This method simply closes the pinhole to diameters below one-quarter airy unit to increase the lateral resolution. This, together with complex real-time deconvolution, is suggested to lead to approximately 140 nm lateral resolution. We have now applied this to cell foci imaging after irradiation and labeled for γ-H2AX. We observed improved foci resolution with some individual focus leading to multiple foci, as is the case with the Airyscan method (see Supplementary Figs. S9 and S10; http://dx.doi.org/10.1667/RR14594.1.S1). The best lateral resolution obtained was 140 nm (Supplementary Fig. S10). This may be due to the fact that the fluorescence intensity of the Airyscan is maintained throughout the image process, while that of the HyVolution 2 method is significantly reduced due to the need to use an effectively closed pinhole in the confocal beam path (Airyscan does not use a pinhole). It is fair to note that the use of software deconvolution to generate super-resolved images has a significant potential to lead to artefacts, particularly in foci detection (see Supplementary Figs. S9 and S10). However, both of these methods (Airyscan and HyVolution 2) are capable of using all the currently known molecular green fluorescent protein derivatives unlike the STED super-resolution technique, which produces optimum results with only the yellow fluorescent protein. Furthermore, the LSM 880 Airyscan and other similar technologies such as the BioAxial system, are only 25% to 10% of the cost of STED system.

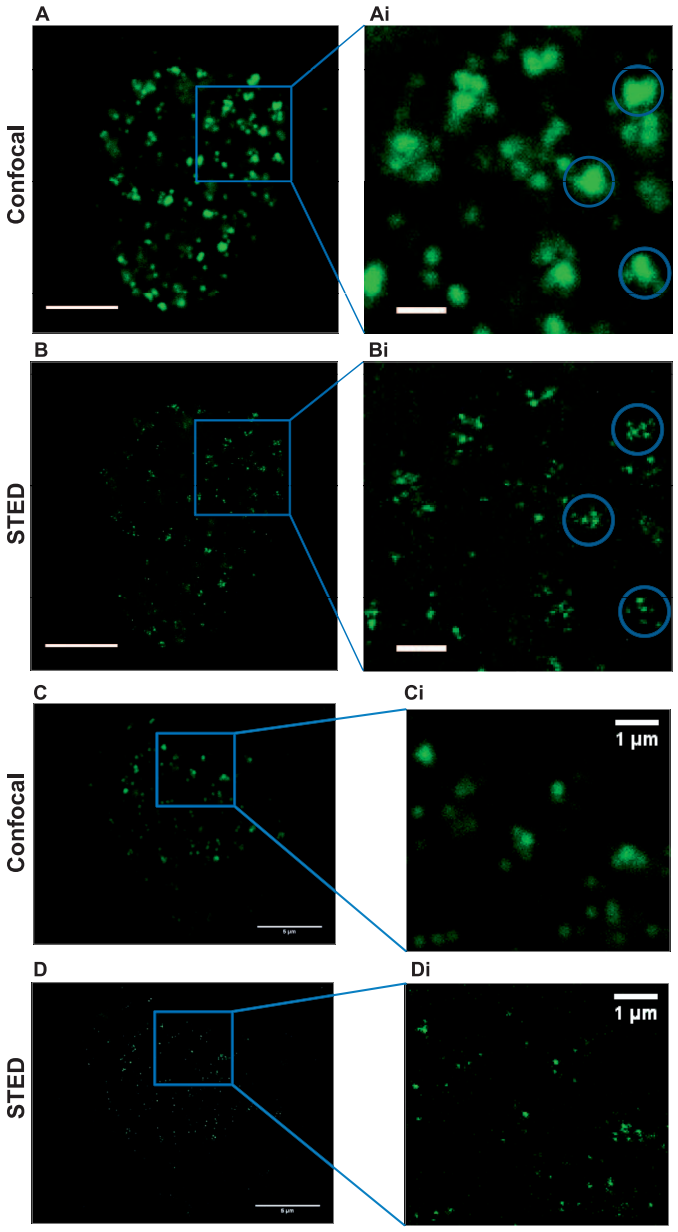

FIG. 3. Fluorescence intensity image of hard X-ray-irradiated CHO cells labeled with primary antibody to γ-H2AX and 53BP1 followed by fluorescently tagged secondary antibody with Alexa Fluor 488. Panel A: Confocal image of γ-H2AX. Panel Ai: Enlarged image of panel A. Panel B: STED image of panel A, same field of view. Panel Bi: Enlarged image of panel B. Panel C: Confocal image of 53BP1. Panel Ci: Enlarged image of panel C. Panel D: STED image of 53BP1. Panel Di: Enlarged image of panel D. Scale bars: 5 µm (for confocal and STED images) and 1 µm (enlarged images).

STED Nanoscopy of γ-H2AX and 53BP1

Figure 3 shows a confocal laser scanning microscopy (Fig. 3A and Ai) and STED nanoscopy images (Fig. 3B and Bi) of 2 Gy hard X-ray-irradiated CHO cells. (Similar data was obtained for soft X-ray irradiation.) Figure 3Ai and Bi are enlarged regions, respectively. The typical γ-H2AX foci formation after hard X-ray irradiation (that is similar to soft X rays) of cells is clearly shown. The origins of sparse foci

TABLE 2
Quantification of Total γ-H2AX Foci (in a Single Cell) after X-Ray Irradiation of HeLa Cells

X-ray dose (repair time)	Confocal	RIF/Gy confocal	Airyscan	RIF/Gy Airyscan	STED	RIF/Gy super-resolution STED
0 Gy (control)	<5	NA	<5	NA	<5	NA
2 Gy (30 min repair)	43 ± 4	20	56 ± 3	28	211 ± 22	105
2 Gy (5 h repair)	8 ± 1	4	20 ± 1	10	53 ± 4	26

Notes. Radiation-induced foci (RIF) determined by dividing radiation dose by foci count. Foci counting leads to ±10% counting error in the super-resolution data and the confocal data.

outside the nucleus are unknown and may be an artefact of nonspecific staining of the fluorescently tagged secondary antibody. It was not possible to stain the cell nucleus with a standard nucleus stain such as DAPI or Hoechst, as these are currently incompatible with certain super-resolution techniques (particularly STED and GSDIM) due to their poor blinking or excited state depletion characteristics. It is worth noting that new fluorescent probes are being developed for live DNA super resolution such as SiR-Hoechst which is a far-red DNA stain (*34*). Upon imaging the same field of view of the sample, all the γ-H2AX could be further resolved into 3 or more foci. Some foci resolved to as many as 7 smaller foci. The STED images show individual focus formation between 60–90 nm with an average of 80 nm (Supplementary Fig. S2; http://dx.doi.org/10.1667/RR14594.1.S1). It is interesting to note that a factor of 2–3 increase in spatial resolution led to more than 6 foci being resolved in many cases. A simple example is shown in Table 2. Foci counting was performed using Imaris software version 8.3.1 (Bitplane AG, Zurich, Switzerland). Although a reduction in the number of foci was reported after a 5 h time point was observed, a significant number of foci remained (20–35%), as detected by the super-resolution methods. It is known that many latent DSBs or replication DSBs, seen as γ-H2AX foci, are formed up to several hours postirradiation through such processes as processing non-DSB-clustered DNA damage into DSBs (with a current estimate of approximately 15–20% relative to immediate DSBs) or through replication DSBs in S/G_2 cells that appear up to several hours postirradiation. In this instance, there are less than 5 foci per nucleus of cells for the control cells (Supplementary Fig. S6). Their fluorescence intensities were not sufficient enough to allow acceptable super-resolution microscopy. It is clear that the increased foci with high intensities observed after ionizing irradiation are primarily due to DNA damage. An attempt to resolve foci from control nonirradiated cells also showed each focus resolving to less than 3 foci. It is likely that foci from nonirradiated cells are due to replication processes.

At first glance, the foci of 53BP1 appear similar in some cells to those of γ-H2AX, as shown in the single-labeled confocal images (Fig. 3C and Ci). However, upon careful examination, the dual-labeled cells show a different foci distribution across the cell nucleus. Furthermore, the foci or punctates in some cells only resolved to smaller punctates without indicating multiple foci. It is highly likely that these unresolvable foci from 53BP1 are not DNA DSB related, as they can also be seen in some control cells. The single-labeled samples show the super-resolved foci of 53BP1 and γ-H2AX to be somewhat different. To test whether foci of 53BP1 and γ-H2AX directly co-localize we prepared dual-labeled samples with 53BP1 as red and γ-H2AX as green.

Figure 4 shows a dual-labeled γ-H2AX (Alexa Fluor 488 fused secondary antibody) and 53BP1 (SiR fused secondary antibody) in HeLa cells irradiated with hard X rays. Again, the confocal image data shows some overlap of the two channels. It was observed that at the STED level (<100 nm; Fig. 4D and Di), the foci of γ-H2AX and 53BP1 were separated spatially, however, they showed significant overlap in the confocal images (Fig. 4C and Ci). The SiR nanoscopy image data shows that the large foci only resolve into fewer foci than those from γ-H2AX, as shown in Fig. 4C. For example, the degree of co-localization but lack of overlap between γ-H2AX and 53BP1 is reflected in the Manders' overlap coefficient (MOC) (*34–36*), with values between 0 and 1 indicating the extent of co-occurrence between red and green pixels (where 0 is no co-occurrence and 1 is perfect co-occurrence). The coefficient $M2$ is calculated using the green channel first, i.e., if there is a green pixel, is there also a co-localized red one?

The $M1/M2$ values for γ-H2AX with 53BP1 are dissimilar at 0.13/0.38. The fact that $M1$ and $M2$ are not close to 1 in both cases indicates that there is little co-localization between γ-H2AX and 53BP1, in the confocal and STED images.

Three-Dimensional Structured Illumination Microscopy

Figure 5A–Ci shows a structured illumination microscopy image of 2 Gy soft X-ray-irradiated CHO cells labeled for γ-H2AX and 53BP1 using primary and secondary antibodies (see Materials and Methods). The technique gave well-resolved foci similar to those obtained using the STED and Zeiss LSM 880 Airyscan techniques. Again, in this technique, each focus resolved to 3 or more foci. The theoretical resolution achievable with this technique is estimated to be approximately 120 nm, (Supplementary Fig. S3 and S4; http://dx.doi.org/10.1667/RR14594.1.S1), a factor of 2 against wide-field epifluorescence microscopy using approximately 500 nm excitation. Line-width profiles across parts of the image showed resolution of at least 112 nm. 3D-SIM is particularly suited to higher resolving power in the axial direction compared to STED or the Zeiss LSM

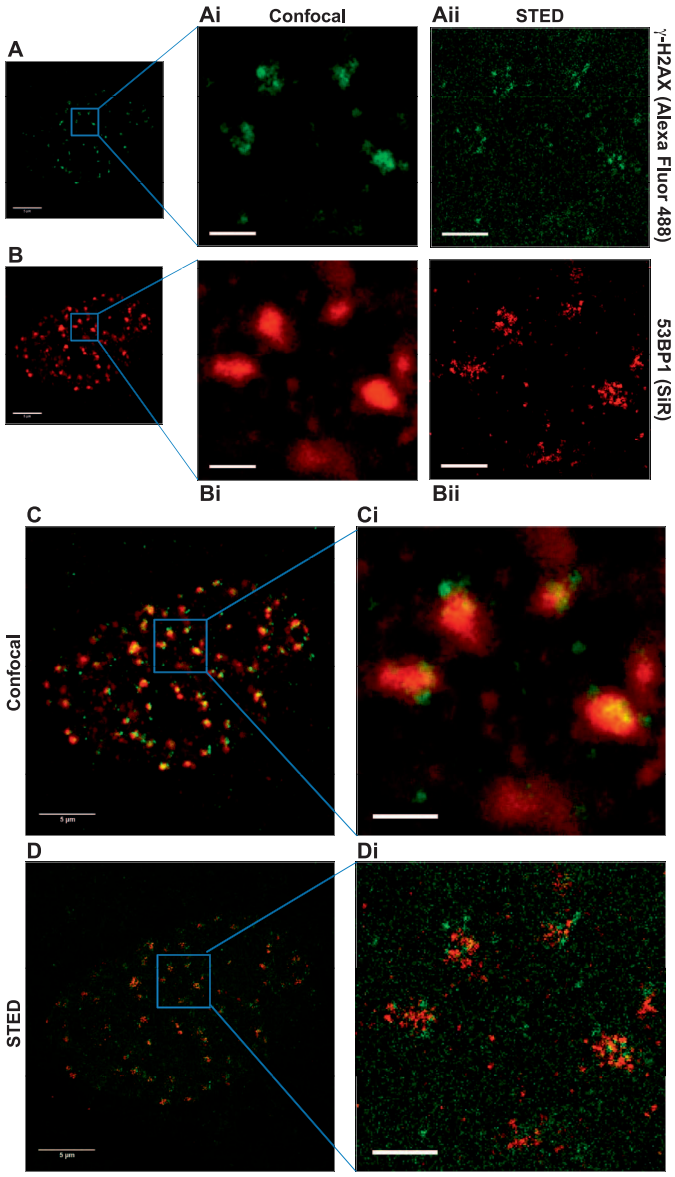

FIG. 4. Dual-labeled fluorescence intensity image of HeLa cells 20 min after hard X-ray irradiation, labeled with primary antibody to γ-H2AX and 53BP1 followed by fluorescently tagged secondary antibody with Alexa Fluor 488 and SiR, respectively. Panel A: Confocal image of γ-H2AX. Panel Ai: Enlarged image of panel A. Panel Aii: STED image of panel Ai, same field of view. Panel B: Confocal image of 53BP1. Panel Bi: Enlarged image of panel B. Panel Bii: STED images of panel Bi, same field of view. Panels C and Ci: Confocal overlay images of γ-H2AX and 53BP1. Panels D and Di: STED images of panels C and Ci, respectively, showing little overlap of the foci. Scale bars: 5 μm (panels A, B, C and D) and 1 μm (panels Ai, Aii, Bi, Bii, Ci, Cii, Di and Dii).

880 Airyscan. This is can be seen in the xz- and yz-profile in Fig. 5, which shows significantly more foci out of the focal plane. This may be critical to obtaining an accurate foci count for radiation dosage purposes. It is worth noting that the large axial resolution from the STED microscope used here (~800 nm) meant any z-profile image was unable to fully resolve the foci in this dimension as observed for the SIM.

GSDIM Nanoscopy of γ-H2AX and 53BP1

Figure 6A–D shows super-resolved images of 2 Gy hard X-ray-irradiated CHO cells labeled for γ-H2AX and 53BP1 using primary and secondary antibodies (see Materials and Methods). At the time of these experiments, the GSDIM technique was only available with a single-color (channel) fluorescence imaging. Thus, both γ-H2AX and 53BP1 were labeled with Alexa Fluor 488 secondary antibodies in separate experiments. As shown in Fig. 6B (γ-H2AX) and 6D (53BP1), with the GSDIM technique large foci are again resolved into several (3 or more) smaller foci. A line-width profile placed across several diffraction-limited foci gives a resolution of approximately 40 nm (see Supplementary Fig. S5; http://dx.doi.org/10.1667/RR14594.1.S1). The GSDIM technique therefore gave the highest resolution image compared to all the other techniques used in this study. This is interesting and unexpected since the technique is based around total internal reflection fluorescence microscopy (TIRF-M) so that increased contrast is afforded by initially eliminating out-of-focus light in the TIRF-M mode. Considering the thickness of the specimen under observation, i.e., ~2 μm overall thickness, (>500 nm to reach the cell nucleus), it is unlikely that a complete TIRF mode will be achieved. Thus, it is more likely that a pseudo-TIRF was operating here to achieve the initial increase in contrast. Nonetheless, the pseudo-TIRF, together with GSDIM, gave γ-H2AX foci resolution that is significantly better than the wide-field epifluorescence and confocal microscopy of approximately 10× improved resolution.

DISCUSSION

In this study, we applied a variety of super-resolution nanoscopy methods and demonstrated how they can improve and resolve down to the 40-nm scale of the DNA DSB and two of its repair proteins. The results complement earlier super-resolution techniques that have been applied to resolving the structure of DNA (*28*). DNA damage repair has also been reported in recent studies using super resolution (*29*). However, as yet the ''structure'' or nanoscopic dimensions of DNA DSBs, as indicated by γ-H2AX, have not been compared using the range of super-resolution microscopies currently available. DNA DSBs are currently analyzed by fragment size using gel electrophoresis such as pulsed-field electrophoresis (PFGE) or comet assay (*37*). Although the background levels of γ-H2AX vary from cell line to cell line, the foci formed after ionizing irradiation is additive and quantitative with a given dose down to the mGy level (*38, 39*). High levels of background γ-H2AX foci may be due to high levels of genomic instability or uncapped telomeres and cellular senescence among other cellular processes. The spatial distribution of foci from such background events was not investigated here, given that the focus was on ionizing radiation-induced effects. However, we note that the super-resolution

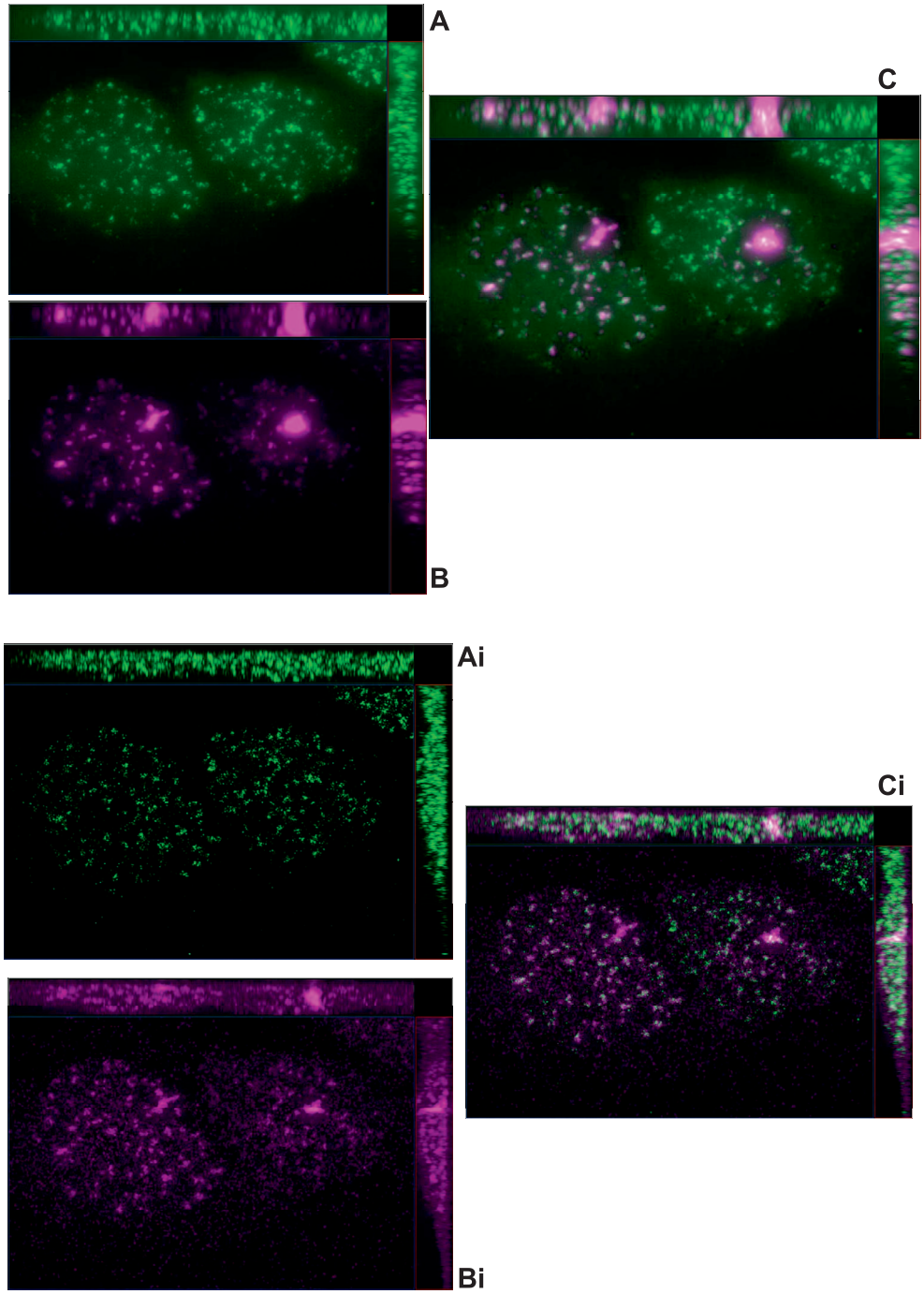

FIG. 5. Wide-field 3D-SIM image of 2 Gy soft X-ray-irradiated CHO cells labeled for γ-H2AX (panel A) and 53BP1 (panel B) and overlay (panel C), with xy-, xz- and yz-projections. Panels Ai–Ci: Super-resolved images of panels A–C, respectively, showing significantly more foci in the z-plane than observed with confocal or wide-field microscopy alone. Field of view is 40 μm for all images.

technique would be advantageous in investigating such cellular processes in general. Imaging of whole chromosomes may also be used to analyze DNA damage after aberration inductions. Premature chromosome condensation (PCC) may also be used to analyze DNA damage with particular emphasis on cell cycle characteristics (*40*). All these techniques are complementary to γ-H2AX analysis in DNA damage studies. Here we show a number of advantages in the application of super resolution and nanoscopy to DNA DSB analysis. First, standard epifluorescence or confocal imaging alone may significantly underestimate the number of foci per cell. Secondly, the given radiation dose against foci formed may be incorrectly scored. Thirdly, the spatial distribution of foci relative to

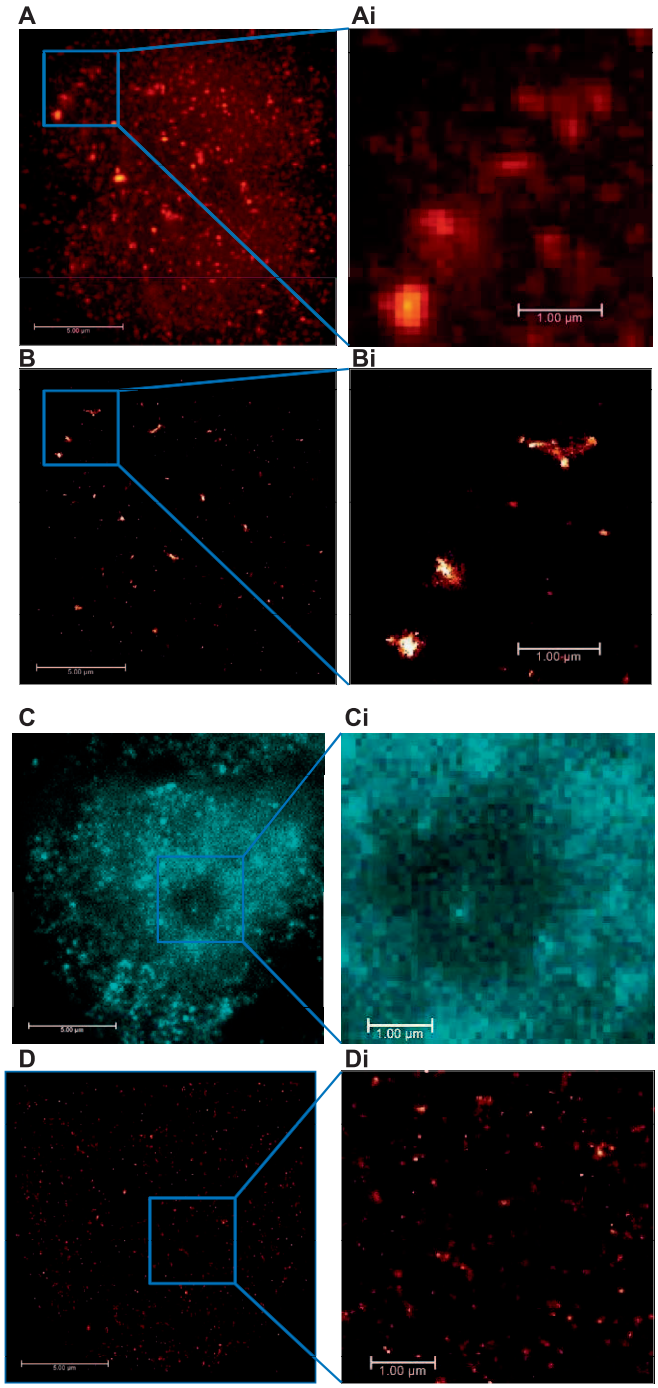

FIG. 6. Fluorescence intensity image of CHO cells 20 min after hard X-ray irradiation, labeled with primary antibody to γ-H2AX and 53BP1, and fluorescently tagged secondary antibody with Alexa Fluor 488. Panel A: Wide-field image of γ-H2AX. Panel Ai: Enlarged image of panel A. Panel B: GSDIM image of panel A, same field of view. Panel Bi: Enlarged image of panel B. Panel C: Wide-field image of 53BP1. Panel Ci: Enlarged image of panel C. Panels D and Di: GSDIM images of panel C. Scale bars: 5 µm (panels A–D) and 1 µm (panels Ai–Di)

each other may be better understood using super resolution. This is likely to aid in the understanding of radiation track structure together with chromatin movement in radiobiology when coupled with different radiation qualities, such as the use of high-LET radiation sources, including ion-particle cell irradiation. We also investigated the effect of radiation quality (hard and soft X rays) on the foci formed, as well as a possible difference between normal and cancerous cell lines (CHO and HeLa, respectively). Such information is not available when using techniques such as PFGE or PCC alone. This is particularly so in the case of PFGE, where high doses are required for the technique to be useful (*2*).

DNA DSBs are also investigated using DNA repair proteins. 53BP1 and Ku70/80 are key DNA damage response (DDR) proteins. It has been suggested that cells with ataxia telangiectasia mutated (ATM)-dependent signaling proteins, such as 53BP1 (an activator of ATM), have a subtle defective DNA DSB repair due to a failure to repair more complex DSBs (*41*), while Ku70 and Ku80 play a critical role in V(D)J recombination. Furthermore, it has been reported that 53BP1 becomes hyperphosphorylated and forms discrete nuclear foci in response to DNA damage and that the foci co-localize at all time points with phosphorylated H2AX (*19*). However, 53BP1 foci may also be formed in response to UV radiation, as well as chemical treatments such as hydroxyurea, camptothecin, etoposide and methylmethanesulfonate (*19*). Thus, it is questionable whether the foci of γ-H2AX and 53BP1 are located in the same spatial coordinates after DNA damage by ionizing radiation. The spatiotemporal characteristics of ionizing radiation-induced DNA damage foci and their relationship to chromatin organization have been well reviewed by Costes *et al*. (*45*). The authors noted that it was important not to equate radiation-induced foci (RIF) of γ-H2AX and 53BP1 with DNA DSBs. The authors also pointed out that not all situations show a one-to-one dose and time dependence of RIF frequency (*45*). We examined γ-H2AX and 53BP1 localization after soft and hard X-ray irradiation of mammalian cells and staining for 53BP1 and γ-H2AX using polyclonal and monoclonal antibodies and fluorescent-labeled secondary antibodies generated for this study. GFP-labeled Ku in stably expressing cells, V15B, was also investigated to confirm DNA damage. It is interesting to note that under nanoscopy imaging conditions with spatial resolution of less than 100 nm, recruitment of Ku, foci of 53BP1 and γ-H2AX do not precisely co-localize, although they appear to co-localize on the 300-nm scale. Additionally, the foci of 53BP1 and γ-H2AX have different morphologies. γ-H2AX foci appear mainly irregular shaped in all the images acquired, while 53BP1 foci are on many occasions circular. Dual-labeled antibody staining allowed us to perform an overlay image registration. It is clear that the foci of 53BP1 and γ-H2AX are spatially distributed differently. This is not surprising since 53BP1 foci formation may occur by several methods that are different from those of γ-H2AX foci formation. We investigated recruitment of Ku70/80 to DNA DSB sites using a GFP-labeled form of the protein in V15B cells. We used both hard X rays and laser (405 nm and 730 nm femtosecond pulses for multiphoton) to induce the DNA damage.

The laser microbeam methodology allowed us to precisely localize the DNA damage and to determine whether the observed florescence from foci is directly due to DNA damage. We observed co-localization of the GFP-Ku protein with immunolabeled γ-H2AX using both confocal and super-resolution imaging, particularly Airyscan (Supplementary Fig. S8; http://dx.doi.org/10.1667/RR14594.1.S1). Here we attempted a three-color experiment, as follows: for green, GFP-Ku (488 nm excitation); for yellow, γ-H2AX (Alexa Fluor 555, 561-nm excitation); and for red, 53BP1 (SiR) (data not shown). Higher fluorescence intensities were observed within the laser-irradiated regions (lines). However, foci formation is not as distinct as those γ-H2AX after low-LET irradiation. This may be due to a number of reasons. For example, the DNA interchelating dye, Hoechst, is required during the laser irradiation, but is known to reduce the quality of super resolution. The higher-than-usual fluorescence intensities observed outside the irradiated areas may be simply due to Hoechst excitation. We are currently investigating the difference between super-resolved foci from low-and high-LET radiation.

We also investigated the foci structure in HeLa cells 20 min after 10 Gy hard X-ray irradiation (Supplementary Fig. S7; http://dx.doi.org/10.1667/RR14594.1.S1). We observed a focus further resolved into several foci, similar to the 2 Gy repair. We speculate that studies using real-time foci imaging together with super-resolution technique would indicate whether initial multiple foci reduce in numbers with time, as well as in their mobility within the cell nucleus. However, these findings need further investigation. Super-resolution imaging of HeLa and CHO cells showed similar foci resolution, i.e., each focus observed in a confocal or epifluorescence microscope resolved into multiple foci. However, there was no statically significant difference between super-resolved foci of HeLa or CHO cells after low-LET irradiation. Also, the repair kinetics, i.e., number of foci remaining after a set repair time or the size of foci, was also similar for CHO and HeLa cells. This is perhaps not surprising since the histone protein phosphorylation process is not known to be impaired in either cell line. Furthermore, although different types of Chinese hamster cells (CHO, V79 and CHW) have been shown to phosphorylate H1 histone subtypes differently during interphase, difference in the phosphorylation of H2 histone has not been studied (*46*). (Although H1 is not part of the nucleosomal core, it plays an important role in nucleosomal stability and aids in higher order chromatin structure.)

The use of super-resolution techniques for imaging cell nucleus and chromosome structures such as nuclear pore and chromatin domains has been previously reported (*29*). We have applied three key super-resolution nanoscopy techniques in this study together with the Zeiss Airyscan and Leica HyVolution 2 pseudo-super resolution. All these techniques showed significant improvement in the spatial resolution of 53BP1 and γ-H2AX imaging (40–140 nm). Techniques such as 4Pi, which have been previously reported, showed only improved resolution and not resolved foci composition as demonstrated in our current study (*42, 43*). Even though GSDIM provided the highest resolution at 30 nm and expected to be similar to other single molecule localization microscopy (SMLM) techniques such as PALM, STROM and their variants, it also has several limitations. In particular, SMLM is currently unable to perform live cell imaging, and thus DNA repair dynamics cannot be studied in real time. This is simply due to the need to use a switching buffer, which is currently not compatible with live cell studies. STED gave a resolution of 80 nm or less in this study. This was a significant improvement on standard confocal microscopy. It is envisaged that the STED technique more likely may allow for live cell imaging, as it is based on standard laser scanning principles when combined with new green fluorescent protein-labeling technologies. That said, the high-depletion light density required for the STED-depleting beams while operating with short pulses (picoseconds) in the visible or near infrared may prove to be a problem for DNA damage and repair studies due to multiphoton processes, which can lead to further cellular damage (*8, 44*). This requires further experimental work to identify the specific limits for STED live cell imaging of DNA damage and repair.

The high-resolution improvement from the use of the SIM technique is highly encouraging towards live cell imaging with increased speed of image acquisition. SIM is expected to give significantly improved axial resolution due to the nature of the technique (see above). The 3D-acquired images of γ-H2AX and 53BP1 foci show well resolved foci within the cell nucleus. Although the 53BP1 foci showed some improvements in the z- (axial) plane, these were not resolved to the same extent as those for γ-H2AX foci. Furthermore, neither the STED nanoscopy nor the Zeiss LSM880 Airyscan method yielded improved z-resolution for the 53BP1. The reasons for this remain unknown and require further investigation.

CONCLUSIONS

We have demonstrated that emerging super-resolution microscopy or nanoscopy, as well as point-spread function-engineered techniques provide improvements to conventional imaging, going beyond 250-nm resolution, for investigating DNA damage and repair. In particular, the resolution improvement of approximately 1.7 provides a means of significantly resolving foci formed by γ-H2AX and 53BP1, which are indicators of DNA DSB and repair processes. Moreover, super-resolution techniques with improved axial (z-) resolution are necessary to account for all foci formed after irradiation of cells and this naturally relates to the 3D structure of DNA and radiation tracks inducing damage. The increased number of foci obtained from the super-resolution techniques indicates that standard epifluorescence and confocal microscopy leads to an underscoring in the number of foci formed within the cell

nucleus. Furthermore, with the use of super-resolution techniques, the foci of 53BP1 and γ-H2AX are spatially distributed differently. Currently, it is difficult to observe Ku70/80 foci during super-resolution imaging for reasons that are unknown.

SUPPLEMENTARY INFORMATION

Fig. S1. Line-width profile of fluorescence intensity image of HeLa cells labeled with primary antibody to γ-H2AX and 53BP1 and fluorescently tagged secondary antibody with Alexa Fluor 488. Comparison of confocal and Airyscan resolution via line-width profiles. Image field of view is 2 μm.

Fig. S2. Line-width profile of fluorescence intensity image of CHO cells labeled with primary antibody to γ-H2AX and 53BP1 and fluorescently tagged secondary antibody with Alexa Fluor 488. Comparison of confocal and STED resolution via line-width profiles. Image field of view is 1.2 μm

Fig. S3. Line-width profile of fluorescence intensity image of HeLa cells labeled with primary antibody to γ-H2AX and 53BP1 and fluorescently tagged secondary antibody with Alexa Fluor 488 and SiR, respectively. Comparison of confocal and SIM resolution via line-width profiles indicating 112 nm xy-resolution and 200 nm z-resolution. Same field of view for the epifluorescence image shows >300 nm resolution. Scale bar = 0.5 μm.

Fig. S4. Line-width profile of fluorescence intensity image of HeLa cells labeled with primary antibody to γ-H2AX and 53BP1 and fluorescently tagged secondary antibody with Alexa Fluor 488 and SiR, respectively. Comparison of wide-field and SIM resolution via line-width profiles indicating 112 nm xy-resolution. Scale bar = 0.5 μm

Fig. S5. Line-width profile of fluorescence intensity image of CHO cells labeled with primary antibody to γ-H2AX and 53BP1 and fluorescently tagged secondary antibody with Alexa Fluor 488. Comparison of wide-field and GSDIM resolution via line-width profiles indicating 40 nm xy-resolution

Fig. S6. Control HeLa cells showing few foci. γ-H2AX labeled with Alexa Fluor 488. Confocal and STED are shown on the left- and right-side panels, respectively.

Fig. S7. HeLa cells 20 min after 10 Gy hard X-ray irradiations. Foci are clearly visible in the STED images (panels Bi and Bii), compared to the confocal images (panels Ai and Aii).

Fig. S8. Laser microbeam (405 nm) irradiations of HeLa cells and comparison between confocal and Airyscan super-resolution imaging. Pretreatment of the cells prior to laser irradiations required loading with Hoechst dye. This may be a source of higher fluorescence intensity observed outside the irradiated lines.

Fig. S9. HeLa cells 30 min after 2 Gy hard X-ray irradiations and comparison between confocal imaging and HyVolution 2. γ-H2AX labeled with Alexa Fluor 488. Foci are clearly visible in the HyVolution 2 images (panels Bi and Bii) compared to the confocal images (panels Ai and Aii). Scale bars on A and B = 2 μm.

Fig. S10. HeLa cells 30 min after 2 Gy hard X-ray irradiations and comparison between confocal imaging and HyVolution 2. γ-H2AX labeled with Alexa Fluor 488. Foci are clearly visible in the HyVolution 2 image (panel B) compared to the confocal image (panel A). Scale bars on A and B = 1 μm. Comparison of confocal (panel Ai) and HyVolution 2 (panel Bi) resolution via line-width profiles.

ACKNOWLEDGMENTS

We thank Professor Chris Hawes (Oxford Brookes University) for access to the Zeiss LSM 880 Airyscan confocal and Professors Tony Parker and Chris Stubbs (STFC, Rutherford Appleton Laboratory, CLF) for their review and discussion of the manuscript. We also thank Public Health England and Oxford University Radiation Oncology for time on the X-ray instruments where samples were irradiated. We thank Professor Dr. Dik van Gent (Department of Cell Biology and Genetics, Erasmus MC), who kindly provided the V15B cells. This work was supported by the STFC through the provision of access to laser laboratories at the Central Laser Facility, Octopus, Rutherford Appleton Laboratory. Support was also provided by Laserlab-Europe (no. EU-H2020 654148).

Received: July 29, 2016; accepted: September 20, 2017; published online: October 20, 2017

REFERENCES

1. Hall EJ, Giaccia AJ. Radiobiology for the radiologist. 7th ed. Philadelphia: Lippincott Williams & Wilkins; 2012.
2. Botchway SW, Stevens DL, Hill MA, Jenner TJ, O'Neill P. Induction and rejoining of DNA double-strand breaks in Chinese hamster V79-4 cells irradiated with characteristic aluminum K and copper L ultrasoft X rays. Radiat Res 1997; 148:317–24.
3. Jenner TJ, Cunniffe SMT, Stevens DL, O'Neill P. Induction of DNA-protein crosslinks in Chinese hamster V79-4 cells exposed to high- and low-linear energy transfer radiation. Radiat Res 1998; 150:593–9.
4. Melvin T, Botchway SW, Parker AW, O'Neill P. Induction of strand breaks in single-stranded polyribonucleotides and DNA by photoionization: one electron oxidized nucleobase radicals as precursors. J Am Chem Soc 1996; 118:10031–6.
5. Ward JF. The early effects of radiation on DNA. In: Fielden EM, O'Neill P, editors. NATO ASI Series H, Vol. 54. Berlin: Springer-Verlag; 1991.
6. Kadhim MA, Macdonald DA, Goodhead DT, Lorimore SA, Marsden SJ, Wright EG. Transmission of chromosomal instability after plutonium alpha-particle irradiation. Nature 1992; 355:738–40.
7. Rogakou EP, Boon C, Redon C, Bonner WM. Megabase chromatin domains involved in DNA double-strand breaks in vivo. J Cell Biol 1999; 146:905–16.
8. Reynolds P, Anderson JA, Harper JV, Hill MA, Botchway SW, Parker AW, O'Neill P. The dynamics of Ku70/80 and DNA-PKcs at DSBs induced by ionizing radiation is dependent on the complexity of damage. Nucleic Acids Res 2012; 40:10821–31.
9. Cowell IG, Sunter NJ, Singh PB, Austin CA, Durkacz BW, Tilby MJ. gammaH2AX foci form preferentially in euchromatin after ionising-radiation. PLoS One 2007; 2:e1057.
10. Bonner WM, Redon CE, Dickey JS, Nakamura AJ, Sedelnikova OA, Solier S, et al. GammaH2AX and cancer. Nat Rev Cancer 2008; 8:957–67.

11. Kim JA, Kruhlak M, Dotiwala F, Nussenzweig A, Haber JE. Heterochromatin is refractory to gamma-H2AX modification in yeast and mammals. J Cell Biol 2007; 178:209–18.

12. Kinner A, Wu W, Staudt C, Iliakis G. Gamma-H2AX in recognition and signaling of DNA double-strand breaks in the context of chromatin. Nucleic Acids Res 2008; 36:5678–94.

13. Olive PL, Banath JP. Phosphorylation of histone H2AX as a measure of radiosensitivity. Int J Radiat Oncol Biol Phys 2004; 58:331–5.

14. Taneja N, Davis M, Choy JS, Beckett MA, Singh R, Kron SJ, et al. Histone H2AX phosphorylation as a predictor of radiosensitivity and target for radiotherapy. J Biol Chem 2004; 279:2273–80.

15. Rothkamm K, Kruger I, Thompson LH, Lobrich M. Pathways of DNA double-strand break repair during the mammalian cell cycle. Mol Cell Biol 2003; 23:5706–15.

16. McKinnon PJ, Caldecott KW. DNA strand break repair and human genetic disease. Annu Rev Genomics Hum Genet 2007; 8:37–55.

17. Jeggo PA, Lobrich M. DNA double-strand breaks: their cellular and clinical impact? Oncogene 2007; 26:7717–9.

18. Moore JK, Haber JE. Cell cycle and genetic requirements of two pathways of nonhomologous end-joining repair of double-strand breaks in Saccharomyces cerevisiae. Mol Cell Biol 1996; 16:2164–73.

19. Rappold I, Iwabuchi K, Date T, Chen J. Tumor suppressor P53 binding protein 1 (53BP1) is involved in DNA damage-signaling pathways. J Cell Biol 2001; 153:613–20.

20. Panier S,, Boulton SJ. Double-strand break repair: 53BP1 comes into focus. Nat Rev Mol Cell Biol 2014; 15:7–18.

21. Hell SW. Microscopy and its focal switch. Nat Methods 2009; 6:24–32.

22. Gunkel M, Erdel F, Rippe K, Lemmer P, Kaufmann R, Hormann C, et al. Dual color localization microscopy of cellular nanostructures. Biotechnol J 2009; 4:927–38.

23. Gustafsson MG. Surpassing the lateral resolution limit by a factor of two using structured illumination microscopy. J Microsc 2000; 198(Pt 2):82–7.

24. Betzig E, Patterson GH, Sougrat R, Lindwasser OW, Olenych S, Bonifacino JS, et al. Imaging intracellular fluorescent proteins at nanometer resolution. Science 2006; 313:1642–5.

25. Flors C, Earnshaw WC. Super-resolution fluorescence microscopy as a tool to study the nanoscale organization of chromosomes. Curr Opin Chem Biol 2011; 15:838–44.

26. Ribeiro SA, Vagnarelli P, Dong Y, Hori T, McEwen BF, Fukagawa T, et al. A super-resolution map of the vertebrate kinetochore. Proc Natl Acad Sci U S A 2010; 107:10484–9.

27. Beliveau BJ, Boettiger AN, Avendano MS, Jungmann R, McCole RB, Joyce EF, et al. Single-molecule super-resolution imaging of chromosomes and in situ haplotype visualization using Oligopaint FISH probes. Nat Commun 2015; 6:7147.

28. Boettiger AN, Bintu B, Moffitt JR, Wang S, Beliveau BJ, Fudenberg G, et al. Super-resolution imaging reveals distinct chromatin folding for different epigenetic states. Nature 2016; 529:418–22.

29. Britton S, Coates J, Jackson SP. A new method for high-resolution imaging of Ku foci to decipher mechanisms of DNA double-strand break repair. J Cell Biol 2013; 202:579–95.

30. Lukinavicius G, Reymond L, D'Este E, Masharina A, Gottfert F, Ta H, et al. Fluorogenic probes for live-cell imaging of the cytoskeleton. Nat Methods 2014; 11:731–3.

31. Folling J, Bossi M, Bock H, Medda R, Wurm CA, Hein B, et al. Fluorescence nanoscopy by ground-state depletion and single-molecule return. Nat Methods 2008; 5:943–5.

32. Bierwagen J, Testa I, Folling J, Wenzel D, Jakobs S, Eggeling C, et al. Far-field autofluorescence nanoscopy. Nano Lett 2010; 10:4249–52.

33. Pawley JB. Handbook of biological confocal microscopy. 3rd ed. New York: Springer Science Business Media, LLC; 2006.

34. Lukinavicius G, Blaukopf C, Pershagen E, Schena A, Reymond L Derivery E, et al. SiR–Hoechst is a far-red DNA stain for live-cell nanoscopy. Nat Commun 2015; 6:8497.

35. Manders EMM, Verbeek FJ, Aten JA. Measurement of co-localization of objects in dual-colour confocal images. J Microsc Oxford 1993; 169(Pt 3):375–82.

36. Dunn KW, Kamocka MM, McDonald JH. A practical guide to evaluating colocalization in biological microscopy. Am J Physiol Cell Physiol 2011; 300:C723–42.

37. Azqueta A, Slyskova J, Langie SA, O'Neill GI, Collins A. Comet assay to measure DNA repair: approach and applications. Front Genet 2014; 5:288.

38. Lobrich M, Rief N, Kuhne M, Heckmann M, Fleckenstein J, Rube C, et al. In vivo formation and repair of DNA double-strand breaks after computed tomography examinations. Proc Natl Acad Sci U S A 2005; 102:8984–9.

39. van Oorschot B, Hovingh S, Dekker A, Stalpers LJ, Franken NA. Predicting radiosensitivity with gamma-H2AX foci assay after single high-dose-rate and pulsed dose-rate ionizing irradiation. Radiat Res 2016; 185:190–8.

40. Rao PN, Wilson B, Puck TT. Premature chromosome condensation and cell cycle analysis. J Cell Physiol 1977; 91:131–41.

41. Dikomey E, Dahm-Daphi J, Brammer I, Martensen R, Kaina B. Correlation between cellular radiosensitivity and non-repaired double-strand breaks studied in nine mammalian cell lines. Int J Radiat Biol 1998; 73:269–78.

42. Bennett BT, Bewersdorf J, Knight KL. Immunofluorescence imaging of DNA damage response proteins: optimizing protocols for super-resolution microscopy. Methods 2009; 48:63–71.

43. Splinter J, Jakob B, Lang M, Yano K, Engelhardt J, Hell SW, et al. Biological dose estimation of UVA laser microirradiation utilizing charged particle-induced protein foci. Mutagenesis 2010; 25:289–97.

44. Meldrum RA, Botchway SW, Wharton CW, Hirst GJ. Nanoscale spatial induction of ultraviolet photoproducts in cellular DNA by three-photon near-infrared absorption. EMBO Rep 2003; 4:1144–9.

45. Costes SV, Chiolo I, Pluth JM, Barcellos-Hoff MH, Jakob B. Spatiotemporal characterization of ionizing radiation induced DNA damage foci and their relation to chromatin organization. Mutat Res 2010; 704:78–87.

46. Wilkinson DJ, Shinde BG, Hohmann P. Cell-specific phosphorylation of H1 histone subtypes among different Chinese hamster cell lines in interphase. J Biol Chem 1982; 257:1247–52.